https://ntrs.nasa.gov/search.jsp?R=20180006191 2019-04-29T08:22:09+00:00Z

Design of Buckling-Critical Large-Scale Sandwich Composite Cylinder Test Articles

Adam Przekop,[1] Marc R. Schultz,[2] and Mark W. Hilburger[3]
NASA Langley Research Center, Hampton, VA 23681

It is well known that the buckling response of thin shell structures can be very sensitive to the presence of small geometric imperfections in the shell. The Shell Buckling Knockdown Factor Project (SBKF) was established by the NASA Engineering and Safety Center to develop new analysis-based shell buckling design recommendations for stiffened-metallic and composite launch-vehicle shell structures. Large-scale buckling tests are used to validate the modeling and analysis methods applied in developing these analysis-based recommendations. Herein, the test-article design methodology for honeycomb-core sandwich composite cylinder validation tests is discussed and 8-ft-diameter cylinder designs are presented. First, the sandwich-composite design space was defined using several nondimensional parameters, and the desired test-article design space was determined by examining the designs of launch-vehicle cylinder structures. Essentially, all test-article designs within certain design parameters were generated and then down-selected based on simple closed-form failure calculations and the nondimensional design-space parameters. Four of these designs span a significant portion of the design space of interest and were predicted to have global buckling as the failure mode. They were selected for higher-fidelity finite-element analysis. It was found that the predicted closed-form buckling loads matched the finite-element analysis well, but that the predicted strains at buckling differed significantly. This difference led to slight redesigns of two of the four test articles. The four selected designs are presented with buckling-response predictions from the closed-form analyses, and from linear and geometrically nonlinear finite-element analyses with perfect geometry and with geometric imperfections.

Nomenclature

A_{ij} = Membrane stiffnesses
A_{ij}^{f} = Facesheet membrane stiffnesses
CTA8.*x* = 8-ft. diameter composite test article where *x* is the ordering number
D_{ij} = Bending stiffnesses
D = Cylinder midsurface diameter
d = Honeycomb core cell size
DIC = Digital image correlation
E = Young's modulus
E_c = Effective core transverse shear modulus

---

[1] Research Aerospace Engineer, Structural Mechanics and Concepts Branch, 8 West Taylor St, Mail Stop 190, AIAA Associate Fellow.

[2] Research Aerospace Engineer, Structural Mechanics and Concepts Branch, 8 West Taylor St, Mail Stop 190, AIAA Senior Member.

[3] Senior Research Engineer, Structural Mechanics and Concepts Branch, 8 West Taylor St, Mail Stop 190, AIAA Senior Member.

$\bar{E}_x, \bar{E}_y$ = Effective facesheet extensional moduli in the axial and circumferential directions, respectively
E_{11}, E_{22} = In-plane extensional moduli in the fiber and matrix directions, respectively
FAW = Fiber areal weight
FEA = Finite-element analysis
FEM = Finite-element model
G = Shear modulus
$\bar{G}_{xy}, \bar{G}_{yx}$ = Effective shear moduli
G_{12} = In-plane shear modulus
G_{13}, G_{23} = Transverse shear moduli in the axial and circumferential directions, respectively
h = Midsurface distance between facesheets $(t_f + t_c)$
IML = Inner mold line
L = Cylinder length
MSFC = Marshall Space Flight Center
NESC = NASA Engineering and Safety Center
OML = Outer mold line
P_{cr} = Global buckling load, defined by Eq. (4)
P_{CS} = Core shear instability load, defined by Eq. (11)
P_{FD} = Facesheet dimpling load, defined by Eq. (10)
P_{FW} = Facesheet wrinkling load, defined by Eq. (9)
R = Cylinder midsurface radius
t_c = Core thickness
t_f = Facesheet thickness
SBKF = Shell Buckling Knockdown Factor Project

ε_{cr} = Axial membrane strain at P_{cr} defined by Eq. (8)
ϕ = Nondimensional parameter in Eq. (4), defined by Eq. (5)
ν = Poisson's ratio
$\bar{\nu}^f_{xy}, \bar{\nu}^f_{yx}$ = Effective facesheet in-plane Poisson's ratios
ν_{12} = In-plane Poisson ratio
σ^{rc}_{cr} = Rigid-core critical facesheet stress, defined by Eq. (6)

I. Introduction

The primary objective of the NASA Engineering and Safety Center (NESC) Shell Buckling Knockdown Factor Project (SBKF) is to develop new analysis-based buckling design guidelines for selected classes of metallic and composite launch-vehicle cylindrical shells.[1] Because these new analysis-based buckling design guidelines can potentially be applicable to the next generation of NASA's launch vehicles, SBKF is considering sandwich composite cylinders.[2,3] For sandwich composite cylindrical shell structures operating primarily under compressive loads, buckling can be a major design consideration, and the critical buckling load is not only influenced by the nominal design, but also by small manufacturing imperfections.[4] Though analysis-based design guidelines are being developed, it is critical to validate the analysis methodology through large-scale cylinder buckling tests. The present work focuses on design and analysis of large-scale buckling-critical sandwich test cylinders representative of flight-like launch-vehicle cylinders. The large-scale testing is to be conducted in a special-purpose test facility at the NASA Marshall Space Flight Center (MSFC). Therefore, the test articles must be designed to meet test facility capabilities, such as the size of a test article that can be accommodated and the maximum load that can be applied.

In this paper, the test-facility design constraints are presented first. Next, a set of nondimensional design parameters describing cylinder design are defined, and the design space of interest was determined based on these parameters. Subsequently, a closed-form analysis approach is discussed and used for the preliminary design of buckling-critical sandwich-composite cylindrical test articles with four designs being selected that span a significant portion of the desired design space. Progressively higher fidelity finite-element models (FEMs) were developed and analyzed next in order to refine the designs. The considered FEMs include variants with the perfect (nominal) and imperfect (as-built) geometric configurations of the sandwich cylinders. FEMs of the test article alone, and of the test article mounted in the test facility are considered. These models are described and results are presented. Finally, concluding remarks are given.

II. Test-Article Preliminary Design and Analysis

The preliminary design and analysis of the test articles utilized classical lamination theory,[5] with the sandwich core considered as a ply, and used closed-form buckling and strength calculations. The considered facesheets were balanced, and either symmetric or unsymmetric. However, all of the facesheets were symmetric about the core, so all of the considered sandwich cylinder walls were balanced and symmetric. Therefore, the laminate stiffness matrix (ABD matrix) of the sandwich shells is simplified because the membrane and bending responses are decoupled, and the extension-shear membrane stiffnesses, A_{16} and A_{26}, are identically zero. Additionally, for such sandwich composites with relatively thick cores and thin facesheets, the bend-twist bending stiffnesses, D_{16} and D_{26}, are quite small and are ignored during the closed-form preliminary design work.

As detailed later in this section, the present effort to develop scaled test-article designs was accomplished using a practical engineering approach. However, an effort to develop a more rigorous approach to such scaled test-article designs is also being undertaken by Balbin, et al.[6]

The test facility is introduced first since it establishes size and loading constraints for the test articles. The design space of interest is determined next, followed by the closed-form failure predictions, and the resulting down-selected preliminary designs.

A. Test-Facility Constraints

The challenge in sizing the subscale specimens is finding physically realizable test-article designs that are representative of present and future launch-vehicle structures, and will fail in global buckling before any other structural failure. Due to physical limitations of the available test facility at MSFC and programmatic constraints, the SBKF composite effort relied on the test of subscale, rather than full-scale (i.e., up to 27.5-ft diameter), structures. Effectively, the test facility is a design constraint for the test articles. The experimental setup with a sandwich composite cylinder installed in it is shown in Figure 1. The test rig was designed to test 8-ft-diameter cylinders with lengths up to at least 10 ft.[7] The test rig is capable of applying the uniform compression up to 1.5x10^6 lbf or combined compression and bending loads. The test articles were mounted via aluminum attachment rings to the green-colored metallic load-introduction cylinders. The top and bottom strut structures (orange beams) and load spiders (blue beams), were connected by eight individually controlled and equally spaced load lines. Different length cylinder test articles can be accommodated in the test frame by changing the lengths of the rods in the load lines. The attachment rings feature groves wider than the end-section thickness of the cylinder, allowing the test article to rest on the bottom surface of this groove. The remaining space in the groove was filled with an epoxy grout. This mounting procedure approximated a clamped boundary condition.

In summary, the subscale sandwich cylinders used in the effort were considered to be *large-scale* (approximately 29% scale as compared to the Space Launch System Core Stage) and were approximately 8.33-ft. tall with an 8-ft. diameter.

B. Test-Article Design Space

To determine the design space, several nondimensional design parameters were used to establish guidance in assessing similarity of test-article designs to full-scale structures of interest. These nondimensional parameters were a combination of nondimensional geometry and nondimensional sandwich stiffness ratios. Though not discussed herein, the nondimensional parameters developed by Nemeth[8,9] were also calculated and considered.

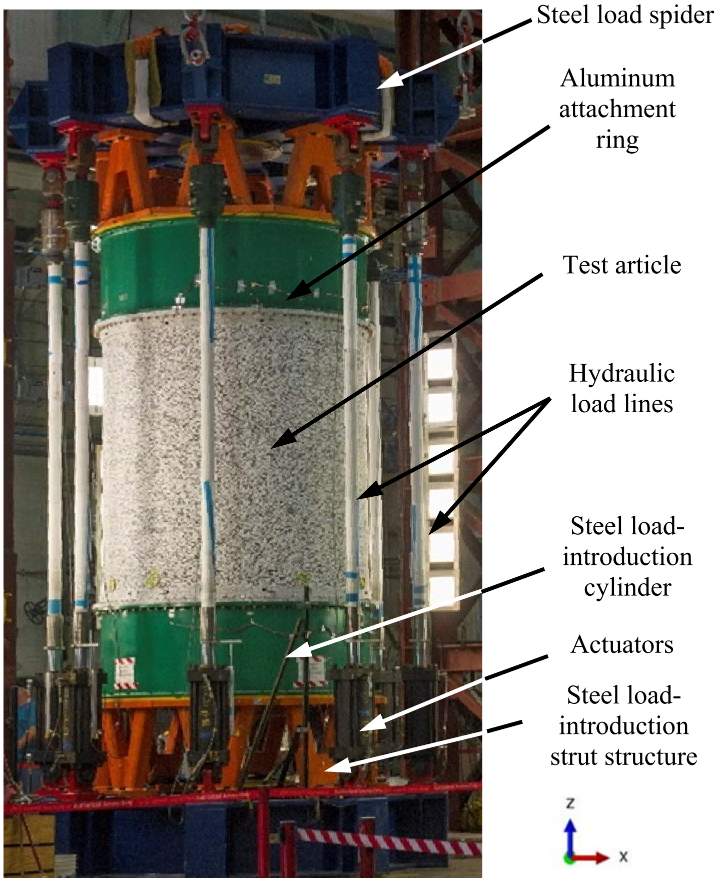

Figure 1. Test facility with a large-scale sandwich composite cylinder installed for testing.

1. *Nondimensional Geometry Parameters*

The geometric parameters are considered first. For isotropic cylinders, the R/t ratio, where R is the shell misurface radius and t is the shell thickness, has long been used as a measure of the *thinness* of the shell and is an important parameter for determining the buckling imperfection sensitivity (e.g., see Ref. 4). However, for orthotropic stiffened or multilayer shells the thickness is replaced by the mean of the stiffness-weighted radii of gyration, which is used as an effective thickness, t_{eff}:

$$t_{eff} = \sqrt[4]{144\frac{D_{11}\,D_{22}}{A_{11}\,A_{22}}} \tag{1}$$

where D_{11} and D_{22} are the axial and circumferential bending stiffnesses, and A_{11} and A_{22} are the axial and circumferential membrane stiffnesses. Therefore, R/t_{eff} is used in this study as a measure of the thinness of the considered cylinders.

The ratio L/D, where L is the test article length and D is the diameter, was considered as a second geometric parameter as this ratio can have an effect on the buckling response of thin cylinders.

2. *Nondimensional Stiffness Parameters*

The relative membrane and bending stiffnesses can affect the buckling response of cylindrical shells, so several nondimensional parameters are used to assess the shell designs. The first parameters are the ratios of the axial-to-circumferential membrane and bending stiffnesses, A_{11}/A_{22} and D_{11}/D_{22}, which can be used as a measure of layup tailoring. These parameters will be greater than unity for axially stiff cylinders, less than unity for circumferentially stiff cylinders, and will be unity for isotropic shells. However, for quasi-isotropic sandwich shells A_{11}/A_{22} will be unity and D_{11}/D_{22} will approach unity.

The in-plane shear and twisting stiffnesses, A_{66} and D_{66} can vary greatly for laminated composite shells. For example, A_{66} and D_{66} will be considerably higher for a quasi-isotropic shell than for a specific orthotropic shell with only axial and circumferential plies. Therefore, the nondimensional stiffness parameters

$$\frac{A_{66}^2}{A_{11}\,A_{22}} \tag{2}$$

and

$$\frac{D_{66}^2}{D_{11}\,D_{22}} \tag{3}$$

are considered as measures of the relative in-plane-shear and twisting stiffnesses. For reference, these parameters will be approximately equal to 0.12 for isotropic materials with Poisson's ratio, ν, of 0.3, and for sandwich shells with quasi-isotropic facesheets. Sandwich shells with cross-ply facesheets will have values less than 0.12.

For the class of sandwich structures considered, ratios of membrane stiffnesses and analogous ratios of bending stiffnesses are very similar. With this similarity, and because the buckling response is largely dependent on the bending stiffnesses, results for the membrane stiffness parameters are omitted for brevity.

C. Sandwich-Composite Failure Predictions

Classical closed-form equations were used to interrogate the most relevant honeycomb-core sandwich composite failure modes. Specifically, the global buckling load, axial membrane strain at buckling, facesheet wrinkling, facesheet dimpling, and core crimping loads were calculated. The global buckling equation of Reese and Bert,[10] which considers transverse shear compliance in the core but neglects the in-plane core stiffness, was used to calculate the global buckling load, P_{cr},

$$P_{cr} = 4\pi\, R\, t_f\, \phi\, \sigma_{cr}^{rc}\left(1 - \frac{1}{2}\frac{\phi\, \sigma_{cr}^{rc}\, t_f\, t_c}{G_{xz}\, h^2}\right) \tag{4}$$

where t_f is the facesheet thickness, t_c is the core thickness, h is the distance between facesheet midsurfaces, G_{xz} is the core transverse-shear modulus in the axial-transverse plane. The parameter ϕ is given by

$$\phi = \text{Minimum: 1 or } \sqrt{\frac{2G_{xz}\left(1+\sqrt{\bar{\nu}_{xy}\,\bar{\nu}_{yx}}\right)}{\sqrt{\bar{E}_x\,\bar{E}_y}}}, \tag{5}$$

and the parameter σ_{cr}^{rc}, the rigid-core facesheet stress, is given by

$$\sigma_{cr}^{rc} = \frac{h}{R}\sqrt{\frac{\bar{E}_x\,\bar{E}_y}{1-\bar{\nu}_{xy}\,\bar{\nu}_{yx}}}. \tag{6}$$

The variables $\bar{\nu}_{xy}$ and $\bar{\nu}_{yx}$ are the effective facesheet in-plane Poisson's ratios, and $\bar{E}_x$ and $\bar{E}_y$ are the effective facesheet extensional moduli in the axial and circumferential directions. The effective Poisson's ratios and extensional moduli are calculated with the assumption that the facesheets are balanced and symmetric, despite the fact that not all considered facesheets were symmetric, and are given by:[5]

$$\bar{E}_x = \frac{A_{11}^f\,A_{22}^f - {A_{12}^f}^2}{A_{22}^f\,t_f} \tag{7a}$$

$$\bar{E}_y = \frac{A^f_{11}\, A^f_{22} - {A^f_{12}}^2}{A^f_{11}\, t_f} \tag{7b}$$

$$\bar{\nu}_{xy} = \frac{A^f_{12}}{A^f_{22}} \tag{7c}$$

$$\bar{\nu}_{yx} = \frac{A^f_{12}}{A^f_{11}} \tag{7d}$$

where the A^f_{ij} are the facesheet membrane stiffnesses. Using these simplified effective properties is reasonable for the case of this buckling prediction because the sandwich shell itself is balanced and symmetric.

The axial membrane strain at buckling, ε_{cr}, is calculated based on P_{cr}, the cylinder axial stiffness, and the assumption that all of the load is carried by the facesheets:

$$\varepsilon_{cr} = \frac{P_{cr}}{4\pi\, R\, t_f\, \bar{E}_x}. \tag{8}$$

The facesheet wrinkling, facesheet dimpling, and core crimping failure loads are calculated based on equations given by Vinson for honeycomb-core sandwich panels[4] and assuming pure compression loading of the cylinders. As such, the facesheet wrinkling load, P_{FW}, is calculated as

$$P_{FW} = 4\pi R t_f \sqrt{\frac{2}{3}\frac{t_f}{t_c}\frac{E_C\sqrt{\bar{E}_x\bar{E}_y}}{1-\bar{\nu}_{xy}\bar{\nu}_{yx}}} \tag{9}$$

where E_c is the effective core transverse shear modulus. The factsheet dimpling load, P_{FD}, is calculated as

$$P_{FD} = 4\pi\, R\, t_f \frac{2\sqrt{\bar{E}_x\, \bar{E}_y}}{1-\bar{\nu}_{xy}\, \bar{\nu}_{yx}}\left(\frac{t_f}{d}\right)^2 \tag{10}$$

where d is the honeycomb-core cell size. Finally, the core-shear-instability load, P_{CS}, is calculated as

$$P_{CS} = 4\pi\, R\, t_f \frac{G_{xz}\, t_c}{2t_f} \tag{11}$$

where G_{xz} is the axial-direction transverse shear modulus. It should be noted that Eq. (11) is simplified for very thin facesheets. This equation was used herein because it predicted more conservative loads than a corresponding equation without this simplification (similar to the equation given in Ref. 9 for core shear buckling in terms of facesheet stress). It is more difficult to justify using the simplified effective properties in the equations for P_{FW} and P_{FD} than it was for P_{cr} because these calculations are meant to predict the performance of the individual facesheets. However, the main objective of this initial design study is to have all other predicted failure loads be significantly higher than the predicted global buckling load, and that these equations can be used in this capacity. The calculated P_{FW} and P_{FD} for all the selected designs were quite high – between five and 80 times P_{cr}. Additionally, four of the five selected designs had symmetric facesheets that satisfy the assumptions, and the fifth design had relatively low membrane-bending coupling that approximates this assumption.

D. Closed-Form Test-Article Design and Limitations

The first step in designing the test articles was to determine the design space of interest by calculating the nondimensional geometry and stiffness parameters for available launch-vehicle cylindrical-shell designs. These designs were a combination of available real, proposed, and SBKF-generated launch-vehicle designs. The nondimensional launch-vehicle geometry parameters are shown as the green squares in Figure 2 with values of L/D that vary from 0.16 to 1.7, and with values of R/t_{eff} that vary from 52 to 121. The low values of L/D represent short cylinders such as skirts, and the higher values represent relatively long cylinders such as interstages. The launch-vehicle nondimensional bending stiffness parameters are shown in Figure 3 and 4 versus R/t_{eff}. In Figure 3, it is seen that most of the launch-vehicle D_{11}/D_{22} ratios were between one and two, but two proposed designs were highly tailored with $D_{11}/D_{22} > 2$. In Figure 4, it is seen that most of the considered launch-vehicle $D_{66}^2/D_{11}\,D_{22}$ ratios vary between 0.024 and 0.16, but most are below the quasi-isotropic sandwich value of approximately 0.12.

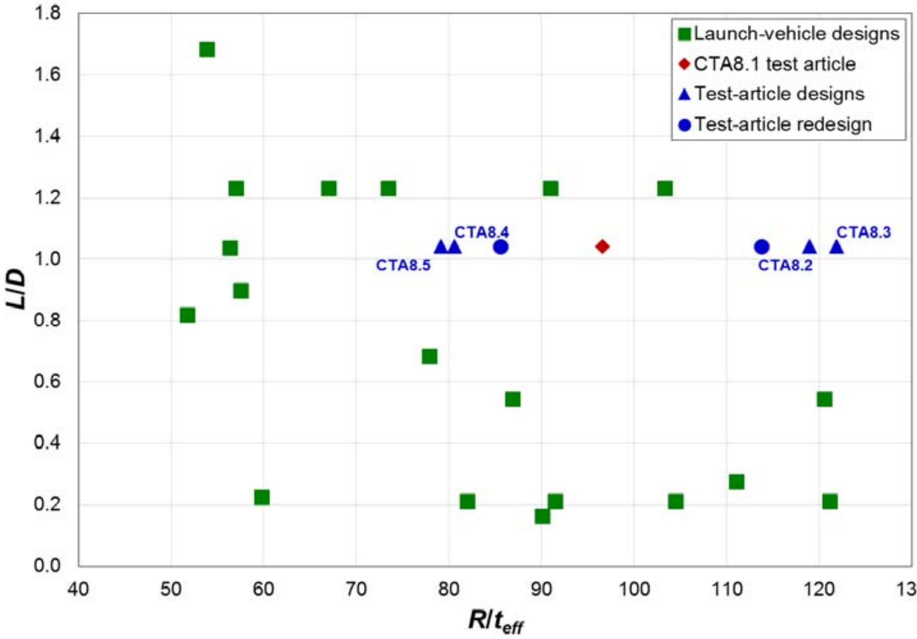

Figure 2. Launch-vehicle and test-article nondimensional geometric parameters.

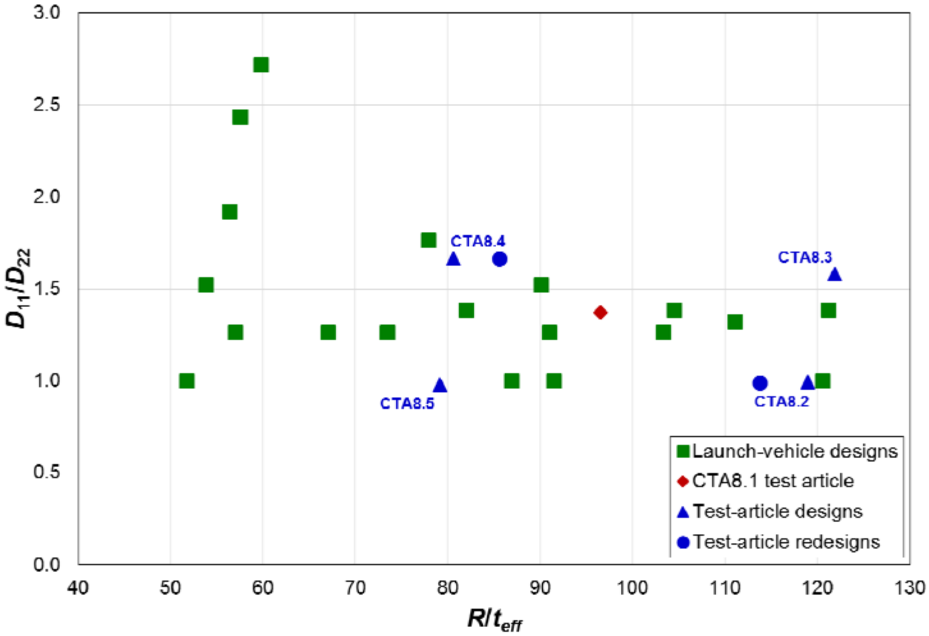

Figure 3. Launch-vehicle and test-article nondimensional bending stiffness parameter D_{11}/D_{22}.

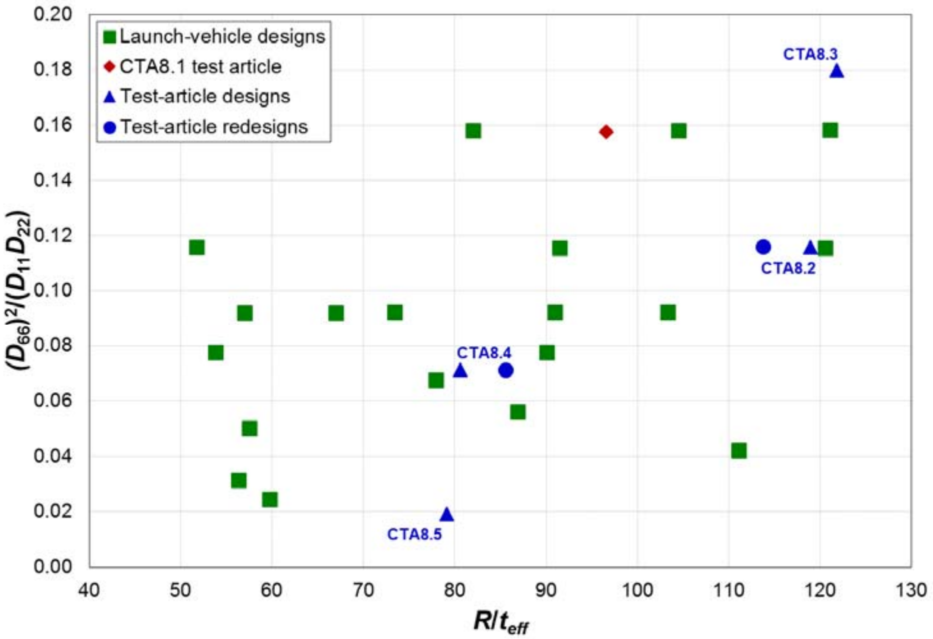

Figure 4. Launch-vehicle and test-article nondimensional bending stiffness parameter $(D_{66})^2/(D_{11}D_{22})$.

The next step in designing the test articles was to generate designs, calculate the nondimensional geometry and stiffness parameters, and use Eqs. 4 and 8-11 to determine the relevant sandwich-structure failure loads. These calculations were made using a SBKF-developed computer code to calculate essentially all potential designs for a given set of parameters. Specifically, the facesheets considered were between two and twelve 0.0054-in.-thick plies of Hexcel IM7/8552-1 graphite/epoxy (145 g/m^2 fiber areal weight (FAW)). Potential ply angles were limited to 0°, 90°, ±30°, ±45°, and ±60°. Hexcel aluminum honeycomb core made of 5056 aluminum alloy with 1/8-in. cells, 0.007-in. cell wall thickness, and a volumetric density of 3.1 lb/ft^3 was selected with thicknesses between 0.1 in. and 0.5 in. at increments of 0.05 in. Additionally, facesheets were constrained to be balanced by grouping the ±30°, ±45°, and ±60° plies. Designs with P_{cr} > 2.0x10^6 lbf, ε_{cr} > 10,000 με, and P_{FW}, P_{FD}, P_{CS} < $1.4\ P_{cr}$ were rejected. This procedure resulted in nearly 100,000 individual designs for further investigation. The number of designs was further reduced by eliminating designs that had no off-axis (angle) plies, had P_{cr} > 1.0x10^6 lbf, or had ε_{cr} > 5000 με; this resulted in approximately 1700 individual designs. It should be noted that the condition that $\varepsilon_{cr} \leq 5000$ με for the accepted designs may seem very conservative, but the ε_{cr} calculation considers only membrane strain, therefore, the strains at buckling in test articles derived from these designs were expected be considerably higher. Finally, designs were down-selected by choosing designs that had nondimensional design parameters that bounded as much of the desired launch-vehicle design space as possible. Five sandwich composite test-article designs, listed in Table 1, were selected for further examination. Their corresponding closed-form failure predictions are shown in Table 2. These results show that for all selected configurations, the lowest failure prediction was associated with global buckling.

Table 1. Closed-form designs.

Design	Facesheet layup	Core thickness, in.	Ply thickness, in.	Fiber aerial weight (FAW)*, g/m^2
CTA8.1	$[\pm45/0/\overline{90}]_s$	0.25	0.0052	n/a
CTA8.2	$[\pm60/0]_s$	0.20	0.0054	145
CTA8.3	$[\pm30/\overline{90}]_s$	0.20	0.0054	145
CTA8.4	$[\pm30/90/0]_s$	0.30	0.0054	145
CTA8.5	$[90/0/90/0/\mp30/90/90/0]_T$	0.30	0.0054	145

* Even though this paper uses the English units, it is customary to express FAW in the International System of Units (SI).

Table 2. Sandwich-composite failure predictions.

Design	P_{cr}, lbf x10^6	P_{FW}, lbf x10^6	P_{FD}, lbf x10^6	P_{CS}, lbf x10^6	ε_{cr}, με
CTA8.1	0.999	6.31	32.6	3.39	5170
CTA8.2	0.779	6.07	24.2	2.71	4825
CTA8.3	0.574	4.44	12.9	2.71	3941
CTA8.4	1.35	7.75	59.1	4.07	4490
CTA8.5	1.22	9.86	95.8	4.07	3920

The first article, designated CTA8.1, was tested as the first SBKF composite test article.[11] This cylinder was designed prior to the present effort using a slightly different approach and fabricated by Northrop Grumman under a cooperative agreement. The nondimensional parameters of CTA8.1 are shown with red diamonds and CTA8.2 through CTA8.5 are shown with blue triangles in Figure 2, 3, and 4. Consider first the nondimensional geometry parameters in Figure 2. Though the considered launch-vehicle L/D ratio spanned a range from quite short to relatively long, a single intermediate value was chosen for the test articles due to the limited number of designs to be manufactured. These test-articles span a significant portion of, but not the entire, launch-vehicle R/t_{eff} design space under consideration. The difficulty in designing the subscale test articles with a low R/t_{eff} ratio results from their tendency to have buckling loads higher than the test-facility load rating, or to reach the compressive material strength limit before buckling. While the latter situation may be desirable for actual designs, such test-article designs would not allow the experimental interrogation of the buckling response as required. Additional limitations were encountered when designing subscale sandwich composite test articles with the high R/t_{eff} ratios due to manufacturing difficulties in producing very thin cores, especially honeycomb cores.

The nondimensional stiffness parameters are shown in Figure 3 and 4. In Figure 3, it is seen that three of the test-article designs are axially stiff and two have essentially equal axial and circumferential stiffnesses, and that these span a significant portion of the launch-vehicle design space. Whereas Figure 4, shows that the considered test-article designs span the entire launch-vehicle design space for $D_{66}^2/D_{11}D_{22}$.

III. Finite-Element Modeling and Detailed Cylinder Design

The closed-form calculations used for the initial test-article design had inherent limitations. For example, the predicted strains were limited to the membrane component only. From a practical engineering standpoint, the analysis was limited to a general sandwich cross-section that did not aid in designing load-introduction features such as the attachment rings or end thickness buildups (later referred to as pad-ups), and was incapable of considering geometric imperfections. Therefore, a further design and analysis effort was warranted for the selected configurations, and the finite-element method was employed as a higher-fidelity modeling and analysis tool.

In this section, the analysis and detailed design for the CTA8.2 test article is presented to illustrate the analysis procedure used for all of the test article designs. The FEMs developed to support the detailed design and analysis effort are also introduced in this section.

A. Detailed Cylinder Design

The test articles were designed to be manufactured using automated fiber placement laying 0.5-in.-wide unidirectional tows and autoclave cure in the MSFC Composite Technology Center. The test-article CTA8.2 acreage design has two quasi-isotropic $[\pm 60/0]_s$ facesheets separated by a 0.20-in.thick honeycomb core. This design results in a relatively high R/t_{eff} of 118, and the axial and circumferential bending stiffnesses being essentially equal ($D_{11}/D_{22} \approx$ 1.0). The high R/t_{eff} was a result of the thin core, and the similar axial and circumferential bending stiffness was achieved by using a quasi-isotropic lamination stacking sequence for the facesheets.

Facesheet buildups at the cylinder ends were designed to mitigate some of the high bending strains associated with the cylinder bending at the boundary and to transfer load into the attachment rings. The pad-ups include up to four plies of the same Hexcel IM7/8552-1 material: two +45° plies and two –45° plies that were interleaved with the acreage plies. The IML facesheet layups in the pad-up regions are shown in Table 3 where pad-up plies are listed in bold font. The OML facesheets were symmetric with the IML pad-ups. The thickness of the pad-up layers was built up away from the IML of the cylinder for both inner and outer facesheets because the cylinder was manufactured on a constant diameter tool.

Table 3. Layups in pad-up regions (pad-up plies in bold).

CTA8.2 cylinder sections measured from cylinder ends, in.	IML facesheet layup
18.0 to 20.0	[60/-60/**45**/0/0/-60/60]
14.5 to 18.0	[60/-60/**45**/0/0/-60/**-45**/60]
13.5 to 14.5	[60/-60/**45**/0/0/**45**/-60/**-45**/60]
0.0 to 13.5	[60/**-45**/-60/**45**/0/0/**45**/-60/**-45**/60]

B. Finite-Element Modeling

An FEM of the composite sandwich cylinder was developed using the commercial general-purpose finite-element analysis (FEA) code Abaqus.[12] The initial FEM for rapid evaluation of the designs included only the sandwich cylinder with the pad-ups and attachment rings, but excluded the test fixture. This initial FEM is identified in Figure 5 as a subset of a detailed FEM that include the test fixture. The test article and attachment rings were modeled using the S4R four-noded reduced-integration shell elements. The sandwich structure was modeled as a layered composite with the individual facesheet plies and the honeycomb core treated as individual layers. Based on mesh convergence studies performed previously for the similar CTA8.1,[3] the mesh size of the composite cylinder was chosen to be 0.5° in the circumferential direction (or approximately 0.4 in.) by 0.5 in. in the axial direction. This model featured approximately 155,000 nodes resulting in approximately 930,000 degrees-of-freedom. The material properties of IM7/8552-1 used in the FEA were E_{11} = 21.2x10^6 psi, E_{22} = 1.82x10^6 psi, and ν_{12} = 0.311. The design of CTA8.2 was modified based on the results of the FEA—the facesheet material was changed from a FAW of 145 g/m^2 to 190 g/m^2. Therefore, the ply thickness of 0.0071 in. was used for the 190 g/m^2 material in the analysis of CTA8.2 and the ply thickness of 0.0054 in. was used for 145 g/m^2 material in the analyses of CTA8.3 through CTA8.5. The material properties of the honeycomb core were E_{11} = 5.8 psi, E_{22} = 2.9 psi, G_{12} = 1.45 psi, G_{13} = 45,000 psi, and G_{23} = 20,000 psi.

Once the designs were interrogated and deemed satisfactory with the simple FEMs, FEMs incorporating the entire test fixture, as shown in Figure 5, were developed to verify that the structural responses with and without the test fixture were similar providing a reasonable estimate of the expected test behavior, including predictions of loads and displacements in the eight load lines. The metallic load-introduction cylinders, seen in Figure 5 as the blue structure, above and below the test article, were modeled using shell elements. These structures were relatively stiff with elements having larger edge sizes of 1.5 in. in the circumferential direction and 2 in. in the axial direction. The load spiders and struts at the very top and bottom of the test setup were modeled with the B31 beam elements with even larger dimensions. The eight vertical load lines were modeled using a single T3D2 truss element for each. The FEM of the cylinder with the entire test setup featured approximately 166,000 nodes resulting in approximately 995,000 degrees-of-freedom.

As mentioned earlier, two geometric variations of each FEM were developed and analyzed. The first used the nominal dimensions of the test cylinder, referred to as the *perfect* model. The second FEM, referred to as the *imperfect* model, had modified node locations to represent the geometric imperfections measured on CTA8.1, as presented in Ref. 10 and shown in Figure 6. While final pretest analysis will be performed using the actual geometry of each manufactured cylinder, the present analysis effort occurred ahead of the cylinder manufacture so the measured imperfections of the similar CTA8.1 were used.

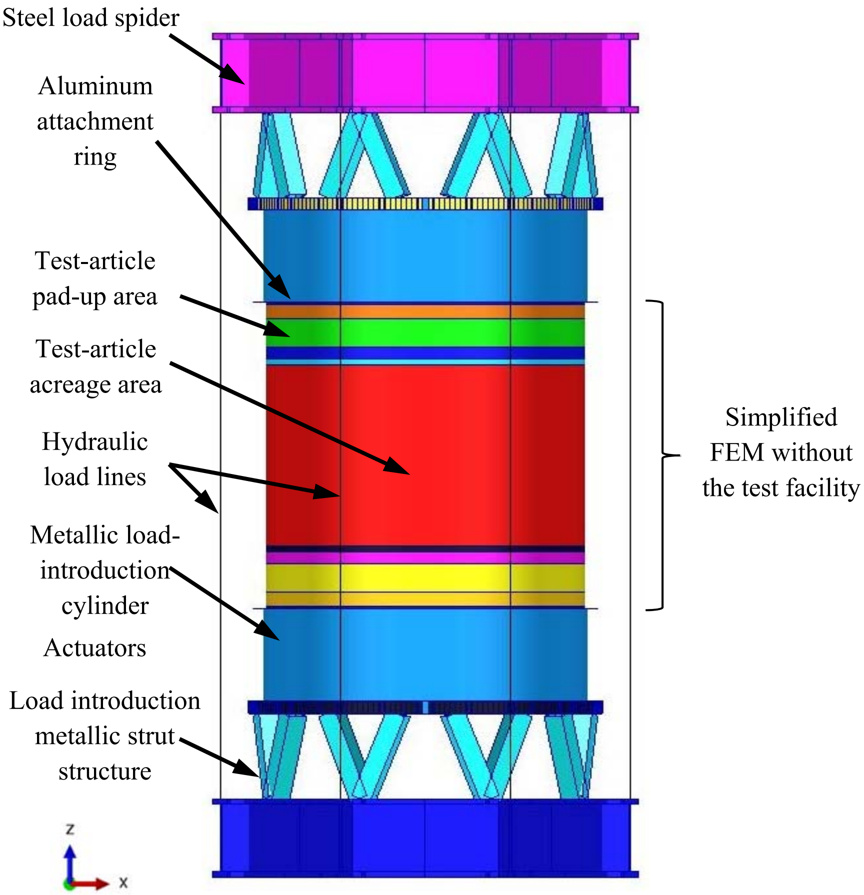
Steel load spider
Aluminum attachment ring
Test-article pad-up area
Test-article acreage area
Hydraulic load lines
Metallic load-introduction cylinder
Actuators
Load introduction metallic strut structure
Simplified FEM without the test facility
z
x

Figure 5. FEM property regions of a composite sandwich test article installed in the test facility.

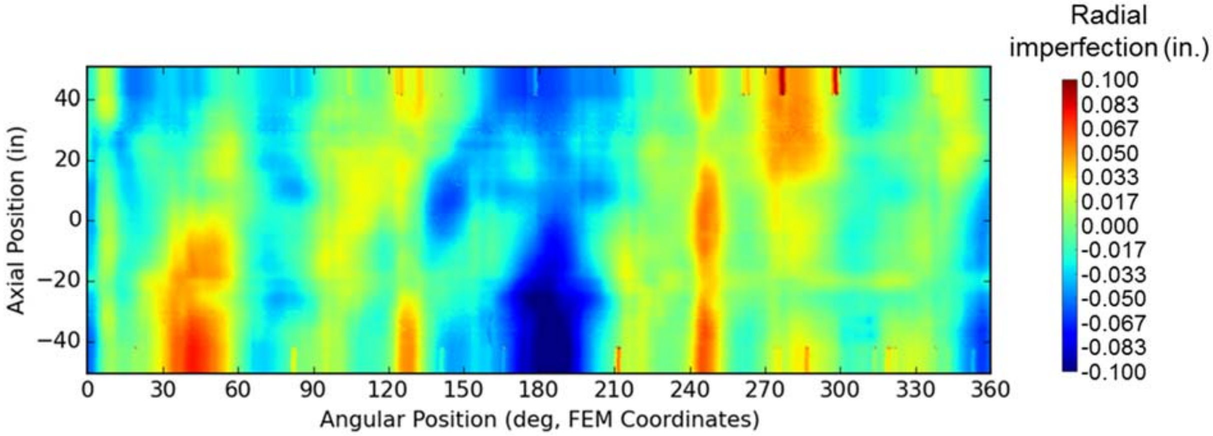

Figure 6. Test-article CTA8.1 measured midsurface radial imperfections.

IV. Finite-Element Analysis and Results

Several FEA methods were used in the effort. Linear eigenvalue analyses were performed first to verify the closed-form buckling load predictions. Quasi-static linear and geometrically nonlinear static analyses were performed to aid in designing the pad-ups, and to assess the effects of nonlinear behavior in the prebuckled response. Finally, implicit transient geometrically nonlinear analyses with quasi-static loading were executed to predict the displacements and strains at incipient buckling and into the postbuckled response regime. For brevity, this section discusses only eigenvalue analysis and transient nonlinear results. However, before the general results are presented, considerations pertaining to the stability of the numerical solution of the perfect models and adjustments of the preliminary designs of two cylinder configurations are discussed.

A. Numerical Stability of Perfect Models

One additional variation of the perfect FEM (i.e., in addition to that discussed in Section III.B) was used in the nonlinear transient analyses for designs CTA8.2 and CTA8.3. These two designs were found to be exceptionally numerically stable in their perfect configurations (the default numerical damping was used in the Abaqus nonlinear transient analyses for all four cylinder designs), which manifested itself in developing an extensive load plateau in the proximity of the buckling load. At the onset of the load plateau, the axial shortening of the cylinder would continue while the corresponding load level would remain almost unchanged, as shown in Figure 7 for CTA8.3. At the same time, the radial deformations would grow in magnitude maintaining a very regular shape and remain stable. The comparison of the predicted radial deformation at the onset of the load plateau and at the end of the plateau for CTA8.3 is presented in Figure 8. The figure shows that in the load plateau region, the radial deformation amplitude grows from 0.124 in. to 0.181 in., or by 46%, while the load level remains virtually unchanged. To remedy this unrealistic numerical characteristic of the perfect model, randomly perturbed meshes, that moved nodes axially and circumferentially while still corresponding to the perfect geometry, were developed. The random perturbation of up to 20% of the element edge size was allowed for each node in the acreage area, i.e., excluding the load-introduction rings and pad-ups. Given the chosen grid parameters, up to ±0.1 in. vertical perturbations and up to ±0.1° (or approximately ±0.08 in.) circumferential perturbations were allowed. It is seen in Figure 7 that the mesh perturbation approach for the perfect model was effective in triggering buckling without the extensive load plateau. The radial deformation obtained from the perturbed mesh model is discussed later in Section IV.C.

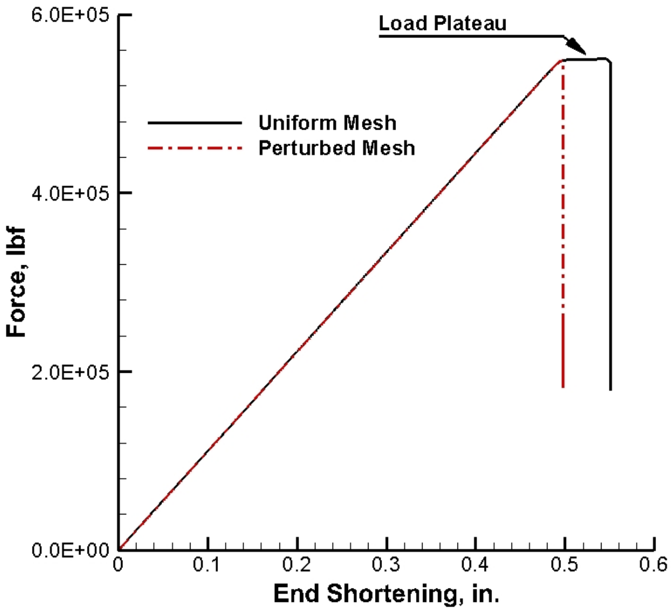

Figure 7. Load plateauing behavior as observed in CTA8.3 analysis.

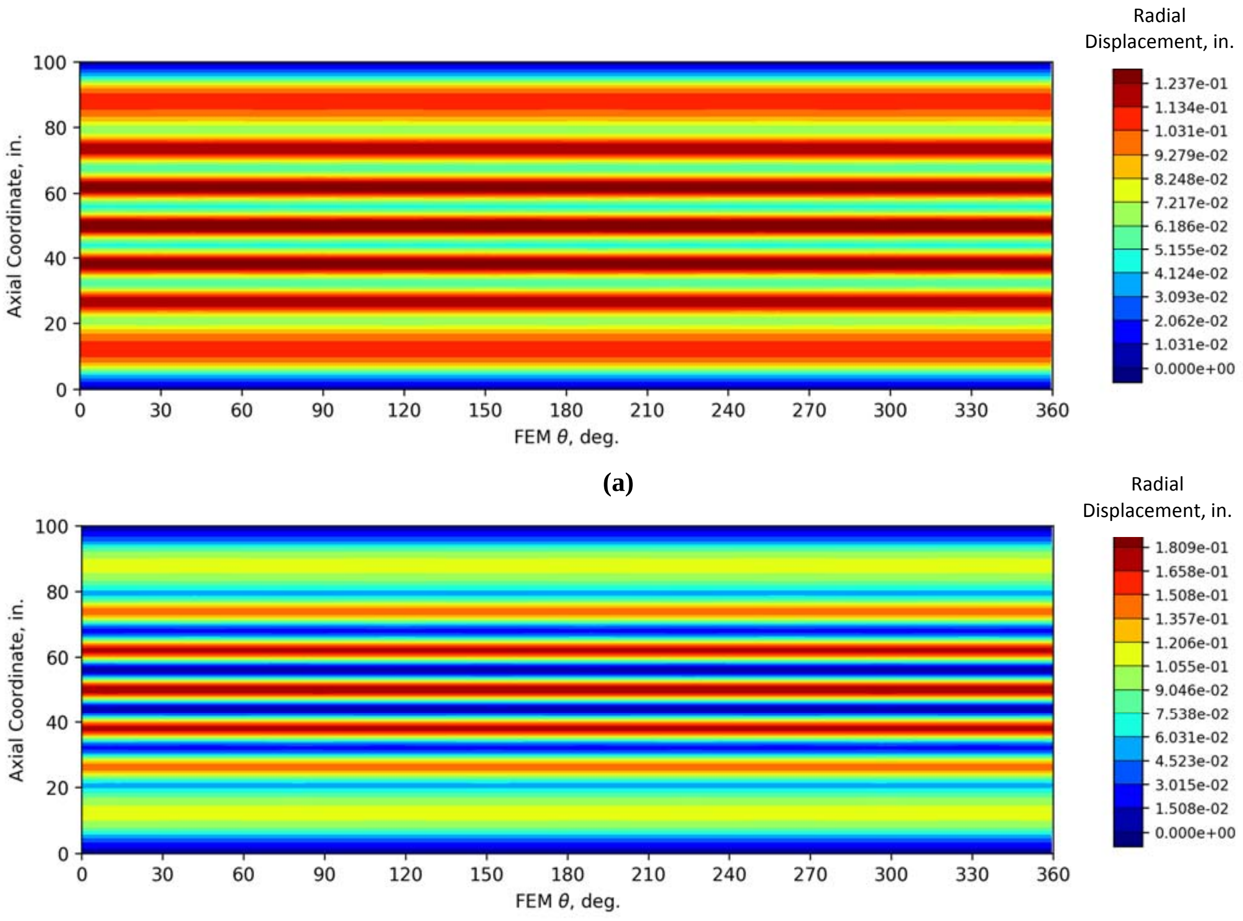

(a)

(b)

Figure 8. Radial displacement: (a) at the onset and (b) end of the load plateau in CTA8.3.

B. Comparison with the Closed-Form Solutions and Design Modifications

This section contains a comparison of the closed-form results with the results obtained from eigenvalue and transient nonlinear FEA, for both perfect and imperfect geometries. It should be mentioned that the comparison was made between the closed-form analyses that considered idealized boundary conditions and only the acreage design, and the FEA as described in Section III that included the attachment rings and pad-ups representing a departure from the idealized end conditions.

The closed-form buckling loads and the finite-element eigenvalue analysis buckling loads for the perfect cylinder configurations are shown in Table 4, and agreed well. For the analyses of the four geometrically perfect initial designs, the linear eigenvalue buckling loads were all within 6% of the closed-form loads. The buckling loads obtained from the nonlinear transient FEA differed slightly from those obtained from the FEA eigenvalue analysis for configurations CTA8.2 through CTA8.4. A more significant difference was obtained for CTA8.5, where the transient nonlinear buckling load was 27.7% higher than that from the eigenvalue analysis. For all designs except CTA8.2, the nonlinear transient solutions predicted higher buckling loads than those obtained from the eigenvalue analyses. As expected and seen in Table 5, the predicted strains at buckling from the closed-form analysis were considerably lower than those predicted from the nonlinear transient FEA. This significant difference was primarily attributed to neglecting the prebuckling bending response in the closed-form analysis, and to the significant axial bending predicted to develop in the prebuckled load range in the FEA.

Table 4. Comparison of buckling loads.

Design	Perfect cylinder, lbf x10^6			Imperfect cylinder, lbf x10^6	
	Closed-form	Eigenvalue FEA	Nonlinear transient FEA	Eigenvalue FEA	Nonlinear transient FEA
CTA8.2	0.779	0.786	0.768	0.773	0.656
CTA8.2*	1.05	0.968	0.962	0.955	0.830
CTA8.3	0.57	0.548	0.549	0.545	0.492
CTA8.4	1.35	1.43	1.51	1.40	1.25
CTA8.4*	1.27	1.26	1.28	1.24	1.10
CTA8.5	1.22	1.25	1.59	1.32	1.15

* Results corresponding to the modified configuration per Table 6.

Table 5. Comparison of axial strains corresponding to buckling loads.

Design	Perfect cylinder, με		Imperfect cylinder, με
	Closed-form	Nonlinear transient FEA	Nonlinear transient FEA
CTA8.2	-4825	-7804	-7639
CTA8.2*	-4960	-5811	-5876
CTA8.3	-3941	-7470	-7638
CTA8.4	-4490	-9556	-8370
CTA8.4*	-4231	-7895	-7912
CTA8.5	-3920	-6192	-5162

* Results corresponding to the modified configuration per Table 6.

Since the FEA predicted undesirably high facesheet strains in CTA8.2 and CTA8.4 (i.e., approaching and exceeding 8,000 με, respectively), these designs were slightly modified as shown in Table 6. Specifically, the lower FAW facesheet material was replaced with the higher FAW 190 g/m^2 material in the CTA8.2 design, and the core thickness was reduced from 0.3 in. to 0.28 in. in the CTA8.4 design. The strengthening of the facesheets in design CTA8.2 and reducing the core thickness in design CTA8.4 were deemed necessary based on the FEA to help ensure global buckling failures and avoid strength failure prior to buckling. The two modifications slightly reduced the design space enveloped by the four designs, as illustrated by the blue circles in Figure 2 through 4. The buckling loads and their corresponding strains for the modified CTA8.2 and CTA8.4 designs are presented in Table 4 and Table 5. Overall, the differences in the buckling strain from the closed-form and nonlinear transient FEA for the final configurations ranged from 14.6% for modified CTA8.2 to 47.2% for CTA8.3. This finding points to a significant limitation of the chosen closed-form solution in predicting the buckling strains.

Table 6. Design modifications for CTA8.2 and CTA8.4.

Design	Facesheet layup	Core thickness, in.	Ply thickness, in.	Fiber aerial weight (FAW)*, g/m^2
CTA8.2	$[60/-60/0]_s$	0.20	original 0.0054 modified 0.0071	original 145 modified 190
CTA8.4	$[\pm30/90/0]_s$	original 0.30 modified 0.28	0.0054	145

Since the actual geometric imperfections of CTA8.2 through CTA8.5 were not known at the time of the analysis, the radial imperfections measured from CTA8.1 (Figure 6) were used for these imperfect FEAs. For all four new designs modeled with the CTA8.1 geometric imperfections, the nonlinear transient analyses produced lower buckling loads than their respective eigenvalue analyses, as showed in Table 4. The buckling load reduction for the final design configurations ranged from 10.8% for CTA8.3 to 15.1% for the modified CTA8.2. It is interesting to note that, while the imperfect buckling loads were predicted to be lower than the perfect buckling loads, the imperfect buckling strains were not consistently lower; the imperfections were predicted to lead to a larger strain-growth rate, which effectively offset the reduction in the buckling load.

C. Displacement and Strain Results

In this section, the results obtained from the nonlinear transient analysis for the FEMs that included the test rig (i.e., from the highest fidelity models employed in the present analysis task) are presented and discussed. The nonlinear analysis results were examined by reviewing the radial and axial cylinder deformations, and the axial and circumferential strain distributions, especially in the vicinity of the buckling load. The strain results received particular scrutiny to ensure that the structures will experience global buckling response prior to a strength failure. The applied load versus cylinder end shortening (i.e., relative displacement of the attachment rings) and versus actuator displacement (i.e., the displacement of the load lines at the actuator) response curves were examined. While the former were a design performance metric, the latter were reviewed to ensure that the test is realized in the available test facility.

The total load applied to the CTA8.2 cylinder by all eight actuators as a function of the actuator displacement is presented in Figure 9. The perfect cylinder is predicted to buckle at 0.959x10^6 lbf and the imperfect cylinder is predicted to buckle at 0.827x10^6 lbf, i.e., 13.8% lower load than the perfect configuration. Both perfect and imperfect cylinders exhibit a nearly linear load versus displacement response. By comparing the buckling load results obtained from the simplified FEMs with the attachment rings only, Table 4, and the buckling loads obtained from the FEMs with the entire load-introduction setup, Figure 9, it is observed that the difference is minimal, i.e., 0.31% - 0.36%. The minimal buckling load differences were consistent with the axial displacement results at incipient buckling, Figure 10, that show that the load-introduction structure is very stiff when compared with the stiffness of the test article. Therefore, the idealized load introduction in the simplified FEM applied by uniform axial displacement of the metallic load introduction rings was nearly identical to that of the test setup.

In the remainder of this section, unrolled contour plots of the strains and displacements are shown to provide a more complete depiction of the cylinder response. Strain results are presented on the surface of the cylinder (OML or IML) producing the minimum axial strain values. Black horizontal lines near the top and bottom of each unrolled plot depict the limits of the pad-up plies.

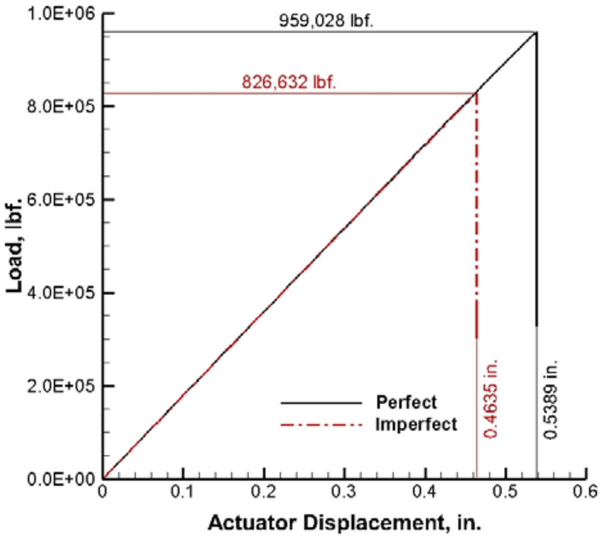

Figure 9. Load versus displacement of the perfect and imperfect CTA8.2 cylinders.

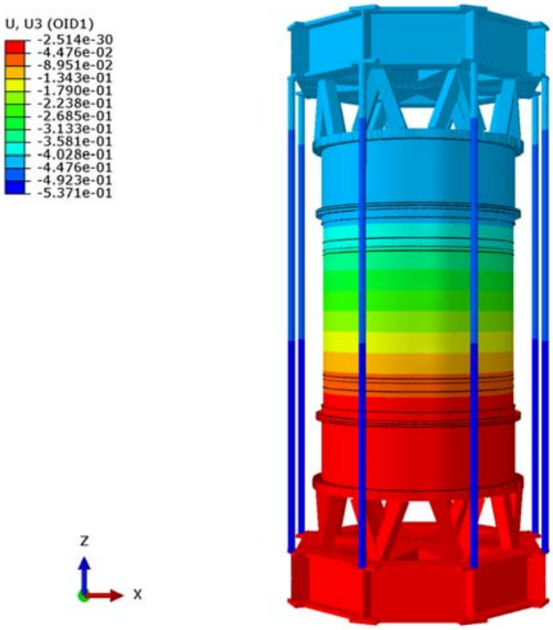

Figure 10. CTA8.2 axial displacement at incipient buckling.

1. *Perfect Model*

The predicted perfect CTA8.2 radial displacements at incipient buckling is presented in Figure 11, and the corresponding axial strain distribution is presented in Figure 12. The perturbed mesh, as described in Section IV.A, was used in the analysis. The radial displacement field at lower loads showed a regular pattern that was qualitatively similar to that shown in Figure 8(a), but as shown in Figure 11, that regular axisymmetric pattern was evolving into a pattern consisting of oval-shaped relatively inward dimples at incipient buckling. The maximum compressive strain of 5811 $\mu\varepsilon$, as shown in Figure 12, was well within the pristine material compressive strain allowable, which for this effort was chosen to be 8000 $\mu\varepsilon$.

The predicted perfect CTA8.3 radial displacements at incipient buckling is presented in Figure 13, and the corresponding axial strain distribution is presented in Figure 14. The perturbed mesh, as described in Section IV.A, was used in the analysis. Qualitatively, both radial displacement and axial strain results in the proximity of the buckling load show very similar characteristics to those of CTA8.2. However, while the maximum radial deformations of CTA8.2 and CTA8.3 are very similar, the latter design shows appreciably higher (29%) axial compressive strains. This response was attributed to the smaller curvatures resulting from higher number of axial half-waves in the CTA8.3 response when compared with the CTA8.2 response.

The predicted perfect CTA8.4 radial displacements at incipient buckling is presented in Figure 15, and the corresponding axial strain distribution is presented in Figure 16. The radial displacement field was distinctly different from that of CTA8.2 and CTA8.3 in that the bending boundary layer was attenuated sooner, and the deformation pattern in the middle of the acreage section was considerable different than that near the ends. Test-article CTA8.4 also had the highest predicted buckling load (see Table 4) and the highest predicted compressive axial strain of 7895 $\mu\varepsilon$ of any of the geometrically perfect configurations considered. While the largest magnitude compression axial strain in Figure 16 was identified in the vicinity of the pad-up, the examination of the subsequent postbuckled solution increment (not shown) indicated that the critical compressive strain location moved away from the pad-ups toward the general acreage area, so that the test article should not fail in the proximity of the padup area, but in the acreage section of interest.

The predicted perfect CTA8.5 radial displacements at incipient buckling is presented in Figure 17, and the corresponding axial strain distribution is presented in Figure 18. The radial displacement field shows the least regular displacement distribution among all four analyzed configurations. Like CTA8.4, the bending boundary layer attenuates quickly. Test-article design CTA8.5 does not have a relative bending stiffness as high as CTA8.3 or CTA8.4 (see Figure 3), thus the compressive axial strain of 6192 $\mu\varepsilon$ was closer to the axial strain value of 5811 $\mu\varepsilon$ for CTA8.2.

2. *Imperfect Model*

The predicted imperfect CTA8.2 radial displacements at incipient buckling is presented in Figure 19, and the corresponding predicted axial strain distribution is presented in Figure 20. The radial displacement field clearly shows two locations where the largest deformations were predicted to develop. The first was located between the 285° and 330° circumferential positions below the midlength of the cylinder. The second, with slightly lower radial displacement amplitudes, was located between 60° and 120°, slightly above the midlength of the cylinder. The compressive strain field was consistent with the radial displacement field and shows the larger magnitude compressive strains occurring in the area of the most dominant outward radial deformation, i.e., at the location where the membrane compressive strain and the compressive strain component due to axial bending are superposed (i.e., at the IML).

The predicted imperfect CTA8.3 radial displacements at incipient buckling is presented in Figure 21, and the corresponding axial strain distribution is presented in Figure 22. The two general areas of large radial displacement growth identified in CTA8.2 were also present in CTA8.3, with the one in the vicinity of the 285° to 330° circumferential position developing faster. This observation indicated that the two configurations show qualitatively similar sensitivity to the same imperfection shape. The largest compressive strain occurs on the IML surface in the area of the most pronounced outward deformation, which wass qualitatively similar to CTA8.2 strain field in Figure 20.

The predicted imperfect CTA8.4 radial displacements at incipient buckling is presented in Figure 23, and the corresponding axial strain distribution is presented in Figure 24. The two general areas where the largest radial deformation grow, as identified in CTA8.2 and CTA8.3 designs, were clearly identifiable in CTA8.4. The larger radial amplitude, unlike in CTA8.2 and CTA8.3, was present in the vicinity of the 60° to 120° circumferential position. However, the largest compressive strain was identified within the deformation in the vicinity of the 285° to 330° angular coordinate. The largest predicted inward and outward radial deformations in the vicinity of the 60° to 120° circumferential position occur side by side at the same axial position of the cylinder. The largest predicted inward and outward radial deformations in the vicinity of the 285° to 330° circumferential position were distributed in both axial and circumferential directions, leading to higher local curvatures and higher bending strains. Thus, both the magnitude of the radial deformation and the specific axial and circumferential distribution were important factors in determining the highest strain levels and their locations. The redesign of CTA8.4 helped to reduce axial strains, this design still produces a maximum compressive strain response very close to the chosen allowable value of 8000 με, namely 7895 με and 7912 με for perfect and imperfect models, respectively. Consequently, the design for CTA8.4 may be further refined.

The predicted imperfect CTA8.5 radial displacements at incipient buckling is presented in Figure 25, and the corresponding axial strain distribution is presented in Figure 26. The maximum predicted radial deformations were clearly concentrated in the area in the vicinity of the 60° to 120° circumferential position. The largest compressive strain was associated with the inward radial deformation at 90° slightly above the midlength. This extreme strain was predicted to occur on the OML surface since this was the side of the cylinder wall where compressive membrane and axial bending components were added.

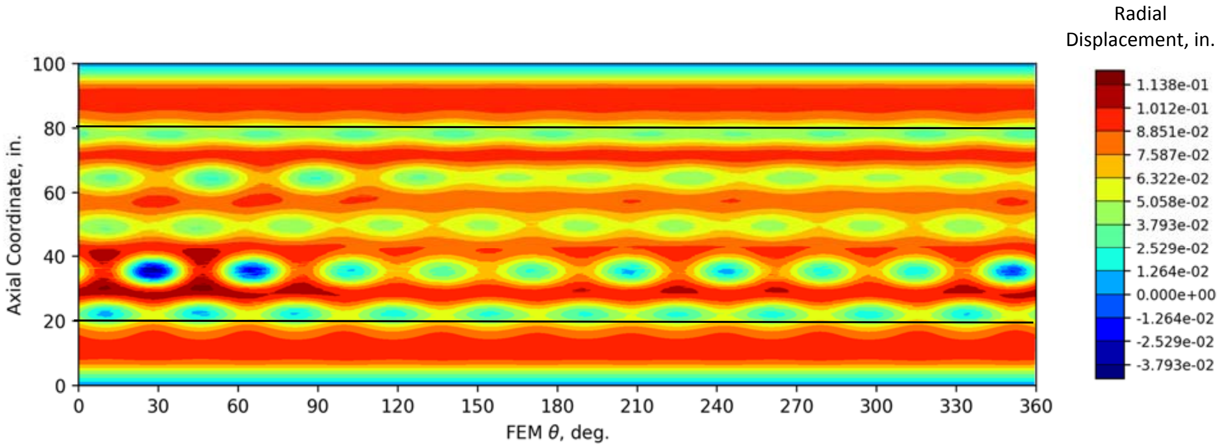

Figure 11. Perfect CTA8.2 radial displacement at incipient buckling.

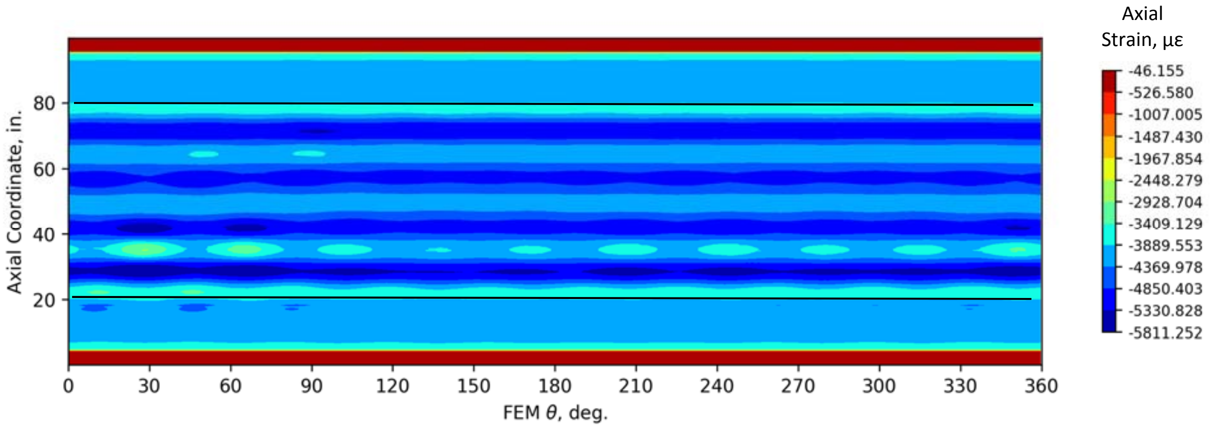

Figure 12. Perfect CTA8.2 IML axial strain at incipient buckling.

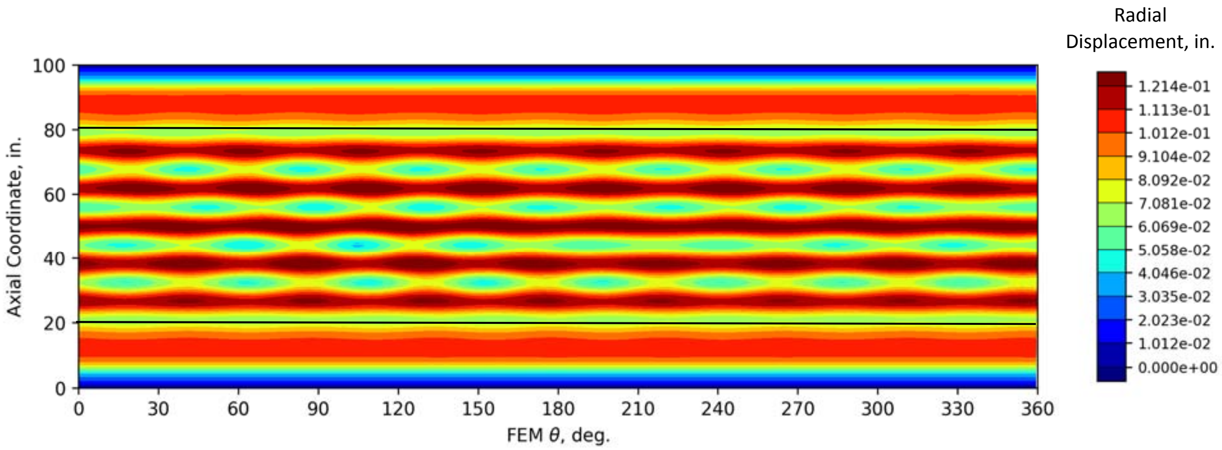

Figure 13. Perfect CTA8.3 radial displacement at incipient buckling.

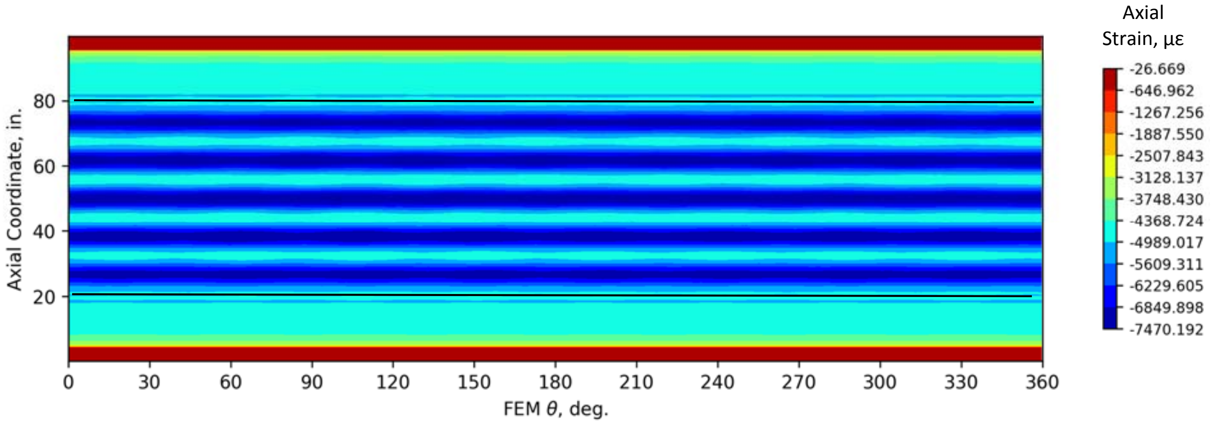

Figure 14. Perfect CTA8.3 IML axial strain at incipient buckling.

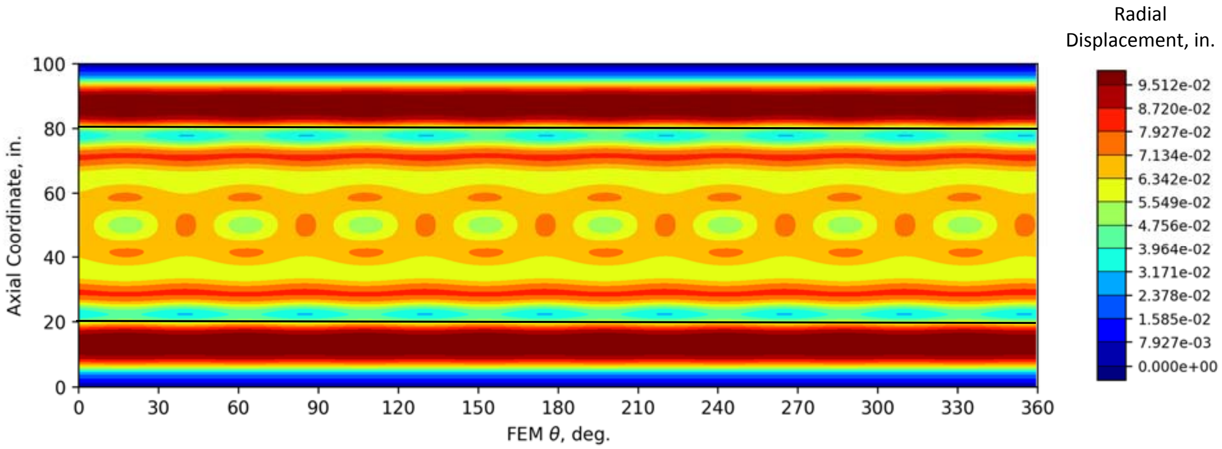

Figure 15. Perfect CTA8.4 radial displacement at incipient buckling.

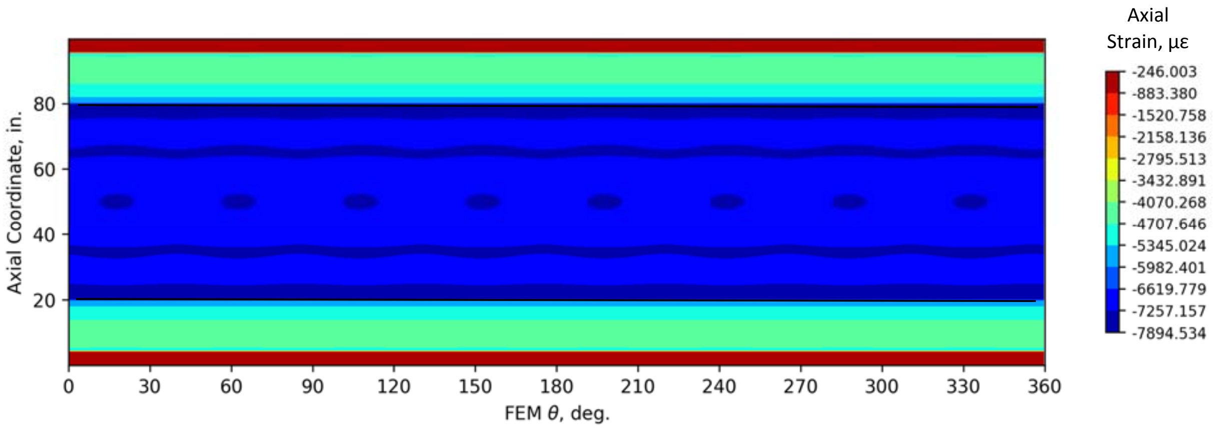

Figure 16. Perfect CTA8.4 OML axial strain at incipient buckling.

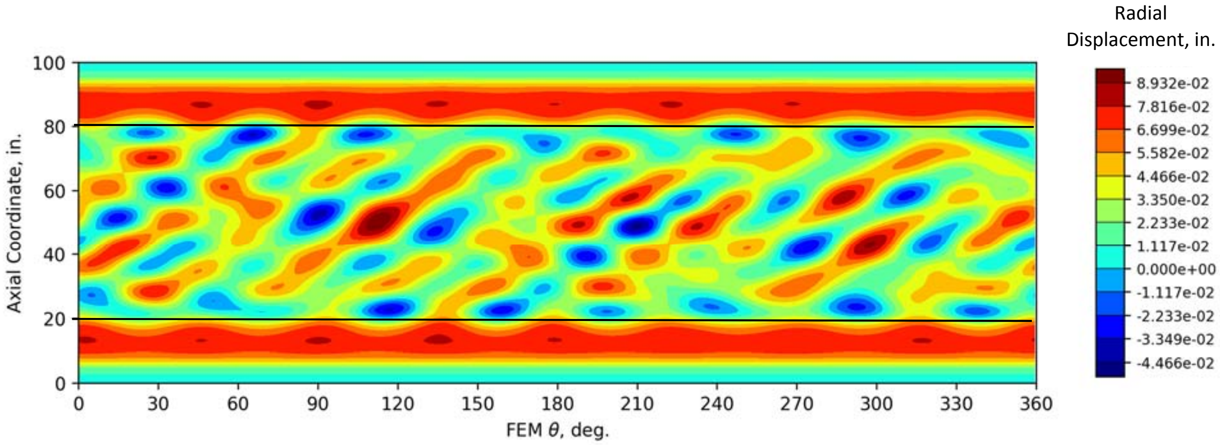

Figure 17. Perfect CTA8.5 radial displacement at incipient buckling.

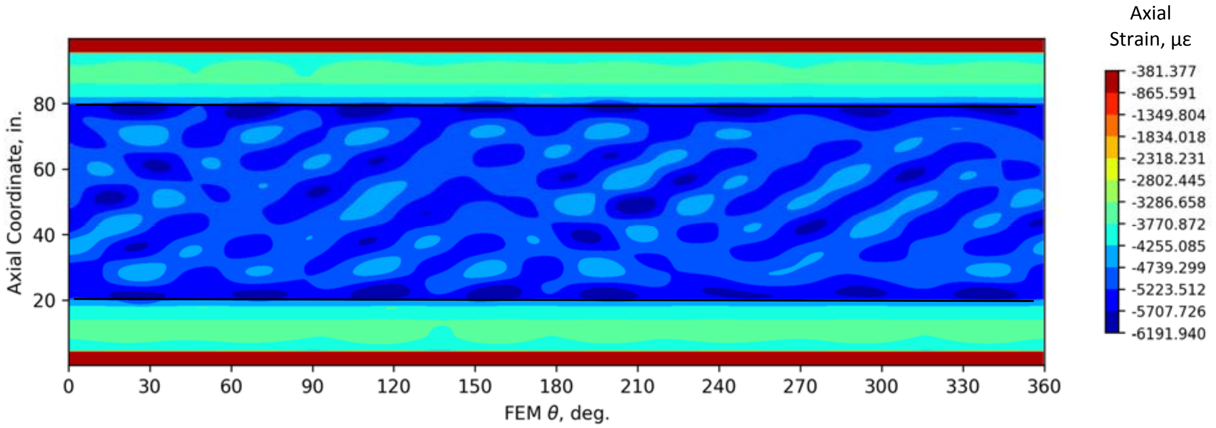

Figure 18. Perfect CTA8.5 OML axial strain at incipient buckling.

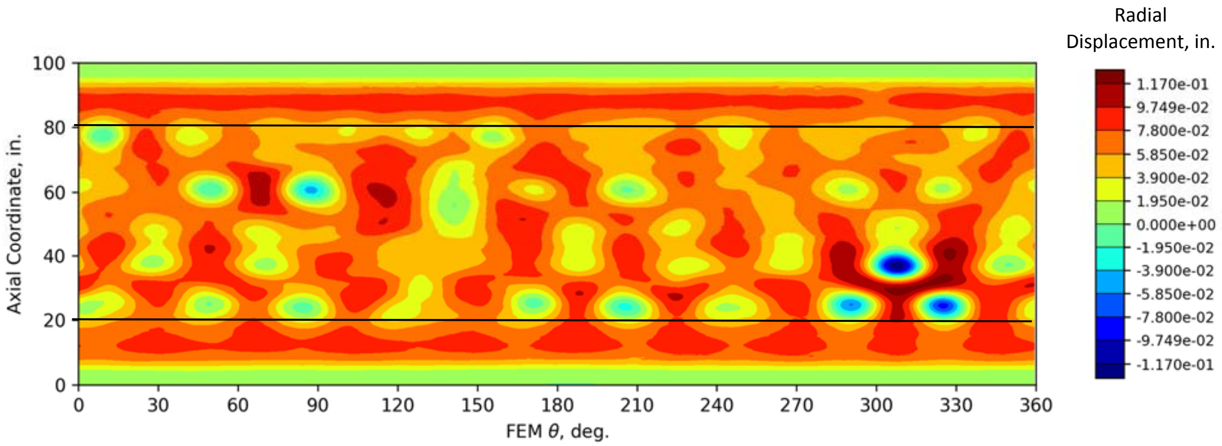

Figure 19. Imperfect CTA8.2 radial displacement at incipient buckling.

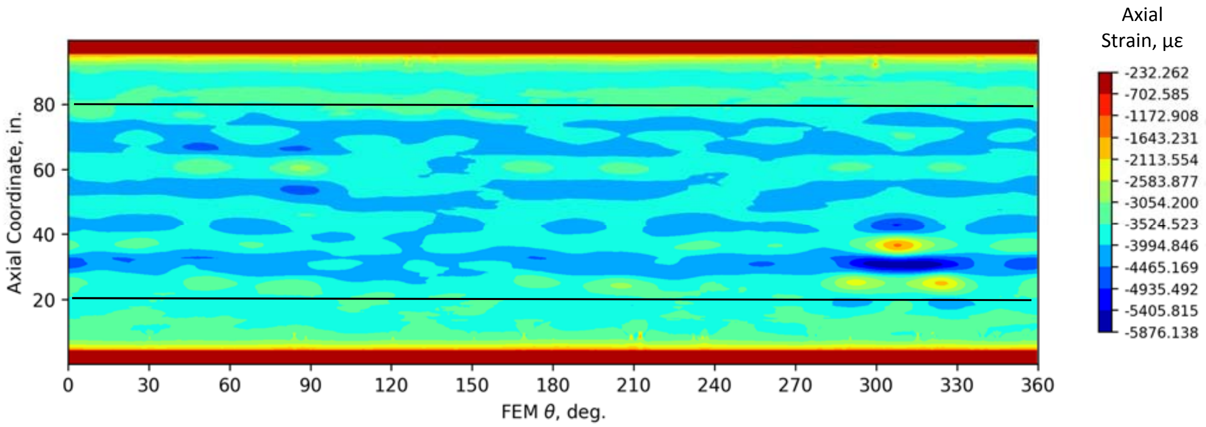

Figure 20. Imperfect CTA8.2 IML axial strain at incipient buckling.

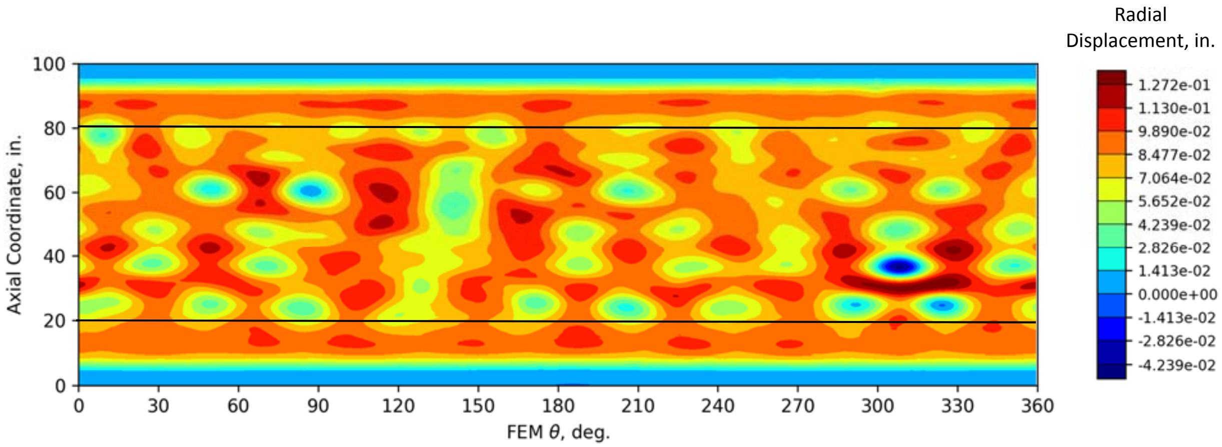

Figure 21. Imperfect CTA8.3 radial displacement at incipient buckling.

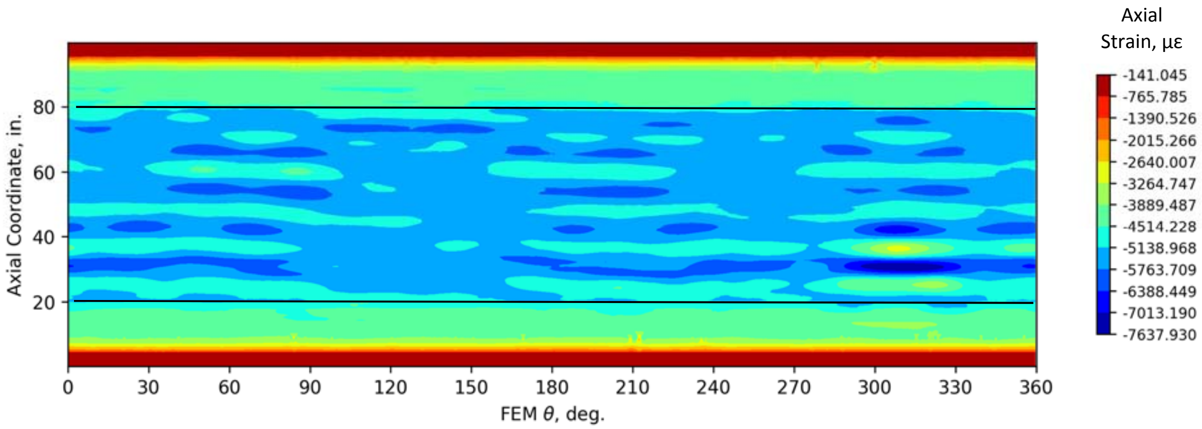

Figure 22. Imperfect CTA8.3 IML axial strain at incipient buckling.

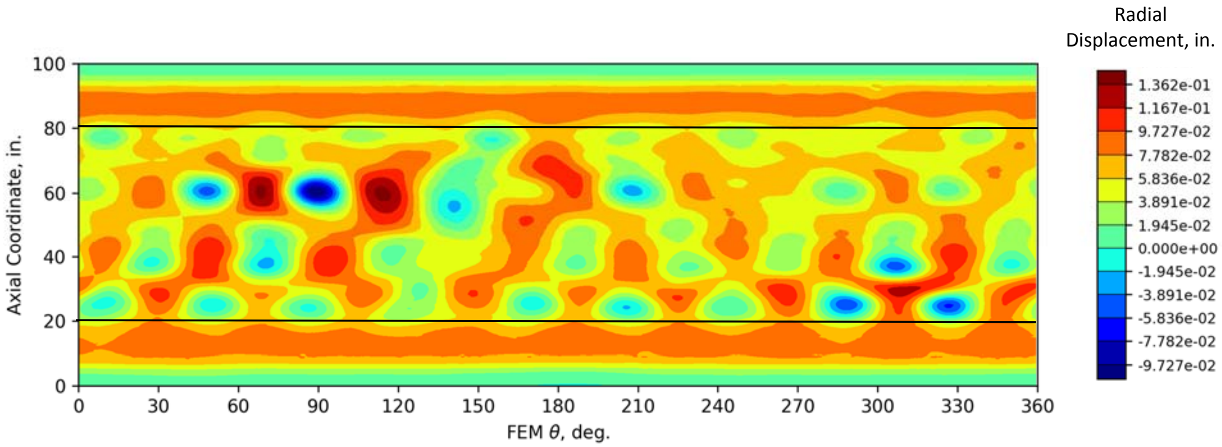

Figure 23. Imperfect CTA8.4 radial displacement at incipient buckling.

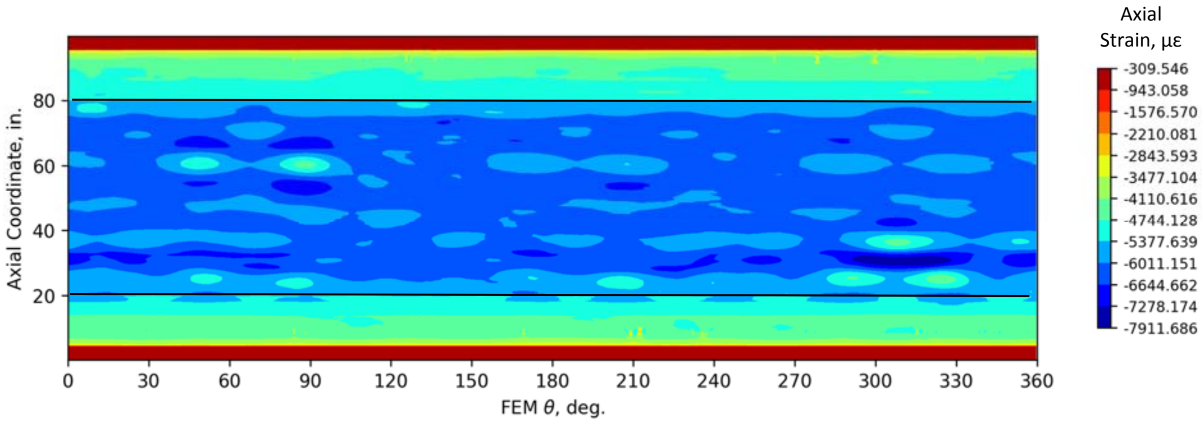

Figure 24. Imperfect CTA8.4 IML axial strain at incipient buckling.

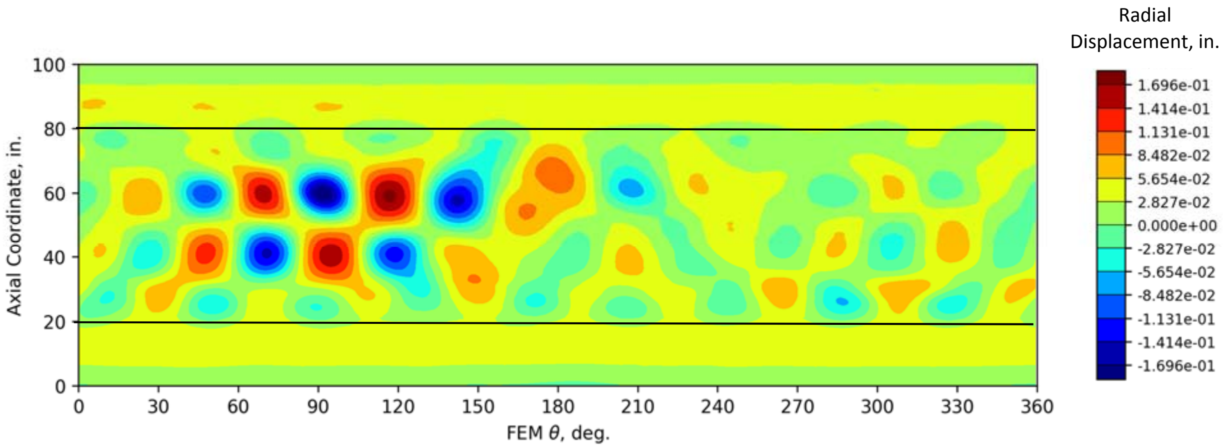

Figure 25. Imperfect CTA8.5 radial displacement at incipient buckling.

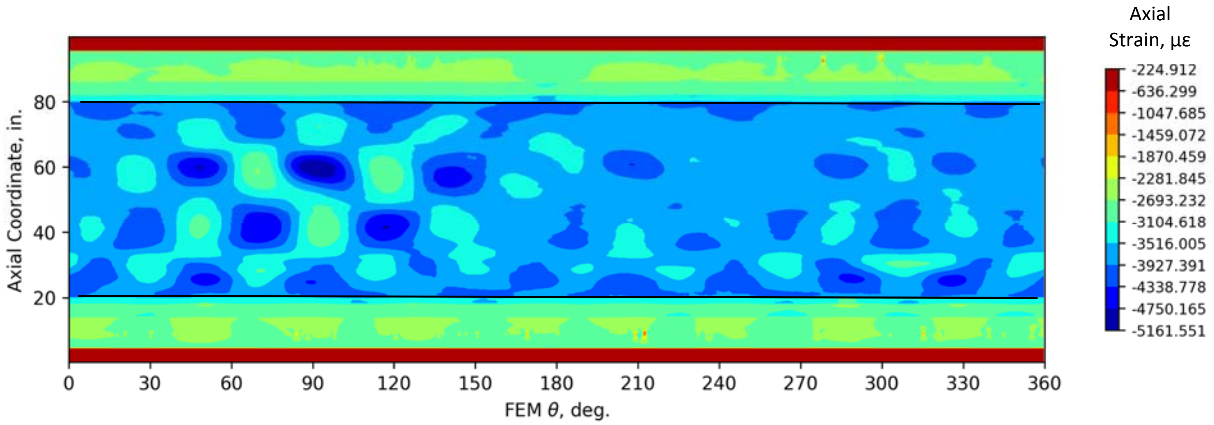

Figure 26. Imperfect CTA8.5 OML axial strain at incipient buckling.

V. Concluding Remarks

The Shell Buckling Knockdown Factor Project has the goal of improving the buckling design guidelines for metallic and composite cylinders through high-fidelity analysis that was validated by large-scale testing. The presented work focused on the design methodology for large-scale sandwich-composite test articles that would provide the valuable data. The challenge was to develop representative buckling-critical scaled test articles.

The first step in the multi-step test-article design process was to define nondimensional geometric and stiffness parameters to determine the design space of interest. Next, a computationally-efficient closed-form process was employed to evaluate a large pool of possible subscale test-article designs. The initial down-selection criteria involved determining designs that have global buckling as the first failure mode with margin. The magnitude of the buckling load and the corresponding membrane compressive strain were constrained next. The span of the design space enveloped by the candidate test-article designs (relative thinness and bending stiffness ratios) was also considered in this step of the process.

Finite-element models were developed for a small number of down-selected candidate test articles. Several finite-element analysis methods were executed, progressing from lower to higher fidelity. These analyses helped identify designs that required modifications as a result of limitations of the closed-form analysis. Further, FEA results allowed evaluation of the effects of the geometric manufacturing imperfections on the buckling loads and the corresponding strains at buckling, which were used as a structural failure criterion. The design of load-introduction ply build-ups and the evaluation of the interaction between test articles, and the test facility were also facilitated by these FEAs. In short, the iterative design process outlined herein was used to develop buckling-critical test articles in the design-space of interest, which could be used for analysis-methodology validation.

Acknowledgements

The authors acknowledge Mr. David Sleight, Mr. Michael Lindell, and Dr. Cyrus Kosztowny (all from the NASA Langley Research Center) for helpful discussions and computer codes provided in support of this work.

References

[1] Hilburger, M. W., "Developing the Next Generation Shell Buckling Design Factors and Technologies," *Proceedings of the 53rd AIAA/ASME/ASCE/AHS/ASC Structures, Structural Dynamics and Materials Conference*, AIAA paper no. 2012-1686, Honolulu, HI, April 2012.

[2] Sleight, D. W., Kosareo, D. N., and Thoma, S. D., "Composite interstage structural concept down select process and results," NASA NF1676L-13769, 2012, pp. 1-15.

[3] Schultz, M. R., Sleight, D. L., Myers, D. E., Waters, W. A. Jr., Chunchu, P. B., Lovejoy, A. E., Hilburger, M. W., "Buckling Design and Imperfection Sensitivity of Sandwich Composite Launch-Vehicle Shell Structures," *Proceedings of the American Society for Composites: Thirty-First Technical Conference*, paper no. 3505, Williamsburg, VA, September 2016, DEStech Publications, Inc., CD-ROM.

[4] Vinson, J. R., *The Behavior of Sandwich Structures of Isotropic and Composite Materials*, Technomic, Lancaster, PA, 1999.

[5] Hyer, M. W., *Stress Analysis of Fiber-reinforced Composite Materials*, McGraw-Hill, New York, 1998.

[6] Balbin, I. U., Bisagni, C., Schultz, M. R., and Hilburger, M. W., "Scaling Methodology for Buckling of Sandwich Composite Cylindrical Structures," *Proceedings of the 59th AIAA/ASME/ASCE/AHS/ASC Structures, Structural Dynamics and Materials Conference*, Kissimmee, FL, January 2018.

[7] Hilburger, M. W., Haynie, W. T., Lovejoy, A. E., Roberts, M. G., Norris, J. P., Waters, W. A., and Herring, H. M., "Subscale and Full-Scale Testing of Buckling-Critical Launch Vehicle Shell Structures," *Proceedings of the 53rd AIAA/ASME/ASCE/AHS/ASC Structures, Structural Dynamics and Materials Conference*, AIAA paper no. 2012-1688, Honolulu, HI, April 2012.

[8] Nemeth, M. P., "Nondimensional parameters and equations for buckling of symmetrically laminated thin elastic shallow shells," NASA TM 104060, 1991.

[9] Nemeth, M. P., "Nondimensional parameters and equations for nonlinear and bifurcation analyses of thin anisotropic quasi-shallow shells," NASA TP-2010-216726, 2010.

[10] Reese, C. D., and Bert, C. W., "Buckling of orthotropic sandwich cylinders under axial compression and bending," *Journal of Aircraft*, vol. 11, 1974, pp. 207-212.

[11] Schultz, M. R., Sleight, D. L., Gardner, N. W., Rudd, M. T., Hilburger, M. W., Palm, T. E., and Oldfield, N. J., "Test and Analysis of a Buckling-Critical Large-Scale Sandwich Composite Cylinder," *Proceedings of the 58th AIAA/ASME/ASCE/AHS/ASC Structures, Structural Dynamics & Materials Conference*, Orlando, FL, January 2018 (submitted for publication).

[12] Abaqus/Standard, Software Package, Ver. 6.14-1, SIMULIA, Providence, RI, 2014.